Available online at www.sciencedirect.com

jmr&t Journal of Materials Research and Technology

www.jmrt.com.br

Review Article

# Effect of multi-pass friction stir processing on textural evolution and grain boundary structure of Al–$Fe_3O_4$ system

*Ghasem Azimi-Roeen*[a,*], *Seyed Farshid Kashani-Bozorg*[b], *Martin Nosko*[c], *Lubomir Orovcik*[c], *Saeid Lotfian*[d]

[a] *Center of Educational Workshops, Isfahan University of Technology, P.O. Box: 8415683111, Isfahan, Iran*
[b] *Center of Excellence for Surface Engineering and Corrosion Protection of Industries, School of Metallurgy and Materials Engineering, College of Engineering, University of Tehran, P.O. Box: 11155-4563, Tehran, Iran*
[c] *Institute of Materials and Machine Mechanics, Slovak Academy of Sciences, Dúbravská cesta 9, 845 13-11 Bratislava, Slovak Republic*
[d] *Faculty of Engineering, University of Strathclyde, Glasgow G1 1XQ, UK*

ARTICLE INFO

*Article history:*
20 November 2019

*Keywords:*
Friction stir processing
Grain refinement
Microtexture
Grain boundary
Nanocomposites
Aluminum matrix composite

ABSTRACT

A mixture of pre-milled $Fe_3O_4$ and Al powder was added to the surface of an aluminum alloy 1050 substrate to obtain hybrid surface nanocomposites using friction stir processing. In situ nano-sized products were formed by the exothermic reaction of Al and $Fe_3O_4$. The reaction is triggered by hot working characteristics of the process. The microstructure and crystallographic microtexture transition and grain boundaries evolution of the fabricated nanocomposite were investigated using optical microscopy, X-ray diffraction, field emission scanning electron microscopy, and electron backscattered diffraction analyses. It is illustrated that matrix means grain size decreased in the specimens, which is processed without and with the introduction of the powder mixture to ~8 and 2 μm, respectively. In addition, high angle grain boundaries showed marked increasing that demonstrates the happening of dynamic restoration phenomenon in the aluminum matrix. Moreover, the fraction of low ΣCSL boundaries showed increasing (remarkably in the presence of hard particles); these boundaries play the main role in dynamic recrystallization. The incorporation of nano-sized products such as $Al_{13}Fe_4$ and $Al_2O_3$ in the dynamically recrystallized aluminum matrix produced a pre-dominantly $Cube_{Twin}$ texture component induced by the stirring function of the rotating tool. As a result, the effect of nano-sized products is constrained.



**Ghasem AzimiRoeen** is an Assistant professor in Center of Educational Workshops of Isfahan University of Technology (IUT), Isfahan, Iran. He received his BSc from Amirkabir University of Technology (2000), MSc degrees (2005) from Isfahan University of Technology and PhD degree (2017) from University of Tehran. He has authored more than 40 papers in journals and conferences. His current research interests include material characterization, friction stir welding and processing, nano-composites, additive manufacturing and surface modification.

* *Corresponding author.*
https://doi.org/10.1016/j.jmrt.2019.10.076

**Seyed Farshid Kashani-Bozorg** is a Professor in the School of Metallurgy and Materials Engineering, University of Tehran. He received his BSc (1984) and MSc degrees (1986) from University of Tehran, and PhD degree (1996) from Imperial College of Science, Technology and Medicine, University of London. He is the author or co-author of more than 60 papers, more than 100 talks at International Conferences on various aspects of surface engineering and characterization of metallic and intermetallic materials. His current research interests include the surface modification, synthesis and characterization of intermetallic materials for rechargeable batteries.

**Martin Nosko** is head of the division of Microstructure of the Surfaces and Interfaces (since January 2017) in the Institute of Materials and Machine Mechanics (IMMM), Slovak Academy of Sciences (SAS). He received his MSc. degrees at 2002 in a field of Material science, physical metallurgy and limit states of materials from Slovak University of Technology in Bratislava a and Ph.D. degree in 2010 from Institute of Materials and machine mechanics Slovak Academy of sciences in a field of Material science, physical metallurgy and limit states of materials. He has authored more than 50 papers mainly in scientific journals focused on the relationship between the parameters of the material preparation, microstructure, and mechanical properties.

He is responsible for coordinating and managing a team of researchers, postdoctoral students, Ph.D. and engineering students working in the field of material characterization. The main focus of his work is attributed to find the fundamental relationships between production, structure, and properties of materials. He independently led and participates in the solution of several domestic and also significant foreign projects focused on both basic and applied research and development.

**Lubomir Orovcik** is a chief of microscopy laboratory at the Institute of Materials and Machine Mechanics (IMMM), Slovak Academy of Sciences (SAS), Bratislava, Slovakia. He received his BSc (2008), MSc degrees (2010) and PhD degree (2015) from Slovak University of Technology in Bratislava, Slovakia. He is the author or co-author of more than 30 papers in journals and conferences. His current work is focused on materials characterization via microscope equipped EDS, WDS, and EBSD detectors. His research has focused on improvement of mechanicals properties of aluminum foam and iron component as well.

**Saeid Lotfian** is a Research Fellow in Materials and Structures at Faculty of Engineering, University of Strathclyde, Glasgow, UK. He obtained his BSc in metallurgy and materials engineering at Iran University of Science and Technology (IUST) in 2002. He graduated in materials science and engineering at Isfahan University of Technology (IUT) in 2005 and got his PhD at Carlos III University of Madrid (UC3M) in 2014. He has authored more than 45 peer-reviewed journal and conference papers. His research has focused on developing novel, smart and multifunctional materials and structures to address known and emerging challenges in the field of marine engineering and renewable energy generation.

## 1. Introduction

The conventional monolithic aluminum alloys are losing their industrial application to aluminum matrix composites (AMCs). The AMCs are increasingly replacing them in various applications including aerospace, renewable energy and, automotive sectors and marine and nuclear engineering [1–4]. Substitution happens because of the excellent physical, mechanical and tribological properties of AMCs such as low thermal expansion coefficient, high strength to weight ratio, stiffness, and good wear resistance [5]. Conventionally AMCs are fabricated using a variety of solid and liquid phase processing techniques, including stir casting [6], powder metallurgy [7] and squeeze casting [8]. Besides conventional processing techniques, the variants of specialized processing techniques were also utilized for AMCs [9–11].

Recently, friction stir processing (FSP) which is a relatively new solid-state process adapted from friction stir welding (FSW), has been widely explored as a surface modification technology [12]. Also, it has attracted much attention as a new process to fabricate metal-matrix nanocomposites (MMCs) [13]. Heretofore during the past decade, a large number of investigations have been carried out to process MMCs by FSP. Recent researches [14–16] showed that the combination of FSP and thermite powder, which undergoes through an exothermic reduction–oxidation (redox) reaction, could be resulted in the formation of AMCs reinforced by in situ $Al_2O_3$ nanoparticles. Various oxide systems such as Al–$Fe_2O_3$ [14], Al–$CeO_2$ [15], Al–$TiO_2$ [17–20], Al–CuO [21] and Al–$Fe_3O_4$ [22] have been used to fabricate the AMCs reinforced by $Al_2O_3$ nanoparticles by using FSP, where reactive mechanisms are utilized to form in situ $Al_2O_3$ particles. The production of aluminum matrix nanocomposites is the result of a chemical reaction between Al and proper metal oxides. The reduction reaction between oxides and Al results in the production of another metal and aluminum oxide. The metal can form as an intermetallic phase with Al or act as alloying constituent inside the Al matrix, which can affect as reinforcements element. The aluminum oxides as the other reaction products, specifically $Al_2O_3$, is a beneficial reinforcement for AMCs [20].

Oxides of iron are a proven candidate in self-sustaining aluminothermic reaction. $Fe_3O_4$ is considered as suitable for its lower cost and high free energy of reaction [23]. The Al–$Fe_3O_4$ system is known for the high exothermic reaction that can be exerted during thermal and/or mechanical treatments according to the following stoichiometric reaction [24]:

$$3Fe_3O_4 + 8Al \rightarrow 4Al_2O_3 + 9Fe \qquad \Delta H^{\circ} = -3021\,kJ \tag{1}$$

The final phases, α-Fe and α-$Al_2O_3$, are formed based on previously mentioned in situ chemical reactions wherein the iron oxide is reduced by aluminum. In relation to the thermite mixture the stoichiometric reaction (1) has been suggested when a powder mix of 8Al and $3Fe_3O_4$ (for both specified in mol.%) is accumulated (i.e., the mass ratio for $Fe_3O_4$/Al is 3.2); nevertheless the final product can be manipulated by non-stoichiometric compositions. Additionally, the presence of extra Al can result in the formation of Al–Fe intermetallics. The reaction products, iron aluminide intermetallics and in situ formed $Al_2O_3$, can act as fine reinforcements. The distribution of them is homogenous within the Al matrix, and they are capable of contributing to strengthening because of their high strength performance.

It is well accepted the FSW/FSP can result in the fabrication of fine/ultrafine and equiaxed grains in the nugget zone due to the dynamic recrystallization [12]. In addition, the preferred orientation are varied around the centerline of stir zone (SZ) which experienced frictional heating and severe plastic

deformation [25]. Texture mainly is induced by the rotating effect of tool shoulder during FSP which cause the compressive and shear influences [26]. Although, (1) it is well known that second-phase particles play an important role in recrystallization. Fine dispersoids tend to hinder boundary motion and slow down recrystallization and grain growth through a Zener drag effect [27,28]; (2) texture can be affected by the presence of nano-sized inclusions within the aluminum matrix, by controlling the particle stimulated nucleation (PSN) and Zener pinning mechanisms [29,30]. Therefore, studying the microstructure transformation and the texture evolution in the center of the sintering zone (mainly in the presence of particles) are of great importance. Another important subject to be noticed is the nature and feature of grain boundaries (GBs) as they have a huge effect on controlling the properties of polycrystalline materials [31]. Kronberg and Wilson [32] proposed the first model to determine the special grain boundaries in 1949 and it known as the *coincidence-site lattice* model. The assumption in their model is based on energy of grain boundary. The grain boundary energy is low when the coincidence of atomic position in both neighbor grains is high. The reason is related to the small number of bonds that are broken across the boundary. It can be explained in case the atoms in the lattice positions state in prefect arrangement when the Gibbs energy of the system is minimum. A grain boundary contain lower energy in case the coincident atoms positioned same as a perfect crystal in compare with non-coincident condition. It means that the two grains are misoriented by a chosen angle $\theta$ around a chosen axis 0. At superposition state related to crystals some atomic sites coincide, which are known as *coincidence sites*. As those sites are deployed regularly, all over the superimposition, they create superlattice, which is named as *coincidence-site lattice* (CSL) [33].

To have a detailed explanation, the misorientation is determined as $\Sigma n$ wherein $n$ value is the reciprocating of coincident lattice sites density with regard to the principal lattice points, which exhibit the data, related to misorientation relationship. $n$ is always odd, and it is possible to calculate it when the plane of the boundary is characterized by symmetric and asymmetric tilt grain boundaries [34]. The CSL model is extensively utilized to categorized GBs into three classes; (i) low angle grain boundaries (LAGBs) while misorientation angle less than 15°. The limitation of 15° is based on the measurements of the contact angle at the grain boundary trace at free surface in bismuth that is exhibited the transition between low to high angle grain boundaries. A recent study measured the migration of planar grain boundaries in aluminum and confirmed a sharp limit between low-angle and high-angle ⟨112⟩ and ⟨111⟩ tilt grain boundaries at 13.6° [33,35–37]. (ii) low ΣCSL boundaries with $3 \leq \Sigma \leq 29$ (i.e., $\Sigma 3^n$ and $n \geq 1$), and (iii) general boundaries which include both random boundaries and high-ΣCSL boundaries ($\Sigma > 29$) [31]. Usually "general grain boundaries" is used when the behavior of the interface is studied. The boundaries with $\Sigma \leq 20$ are known as special boundaries [38]. The low value of $\Sigma$ determines as a special grain boundary. This term can explain the boundaries that display sharp extremes at any property orientation dependence, such as, fracture toughness, diffusivity, the tendency to segregation, migration rate, sliding rate and corrosion rate [33]. Recent orientation mapping studies offered that the materials with a high fraction of low-ΣCSL boundaries, particularly Σ3 boundaries, due to their potential for structural order in the boundary plane exhibit dominant properties [31]. It can be stated that the improvement of certain properties has resulted in special grain boundaries [39].

The objective of the study demonstrated in this article is to evaluate the fundamental concepts of grain boundary evolution and microtexture development in the center of sinter zone of in situ nanocomposites formed by using FSP in Al–$Fe_3O_4$ system. Accordingly, to provide a profound understanding of the grain boundary transformation and crystallographic texture evolution, the electron backscattered diffraction (EBSD) technique was used in conjunction with field emission scanning electron microscopy (FE-SEM).

## 2. Materials and methods

### 2.1. Used materials

To have a consistent explanation of microstructure and varieties of the properties in the final composite produce from $Fe_3O_4$–Al system, a AA 1050 rolled sheet was selected which has 5 mm thickness and contain a high amount of Al (>99%). The nominal chemical composition of the Al rolled sheet is presented in Table 1. The sheet was provided by Arak Aluminum Co., Arak, Iran. To prepare the workpieces, the Al sheets was cut off in the dimensions of $210 \times 70 \times 5\,mm^3$ and a groove was machined in the middle length when the depth and width are 3.5 mm and 1.4 mm, respectively. Afterwards, the milled powder mixture is inserted to the machined grooves. $Fe_3O_4$ (>98% purity with the particle size of ~20–30 nm), and Al (>99%. purity with the average size of ~100 μm) powders were mixed based on the stoichiometric combinations in Reaction (1). The as-received powders morphology is illustrated Fig. 1(a) and (b).

### 2.2. Mechanical alloying

Mechanical milling was used to prepare the powder mixture. They milled for 1 h when the milling carried out by using high-energy planetary mill underneath of the argon (99.999%) atmosphere. Table 2 present the mechanical alloying process

**Table 1 – Nominal chemical composition of AA1050 sheet (wt.%).**

| Al | Zn | Cr | Mg | Mn | Cu | Fe | Si |
|---|---|---|---|---|---|---|---|
| Base | 0.0097 | 0.0041 | 0.0017 | 0.0061 | 0.0123 | 0.272 | 0.206 |

**Table 2 – Mechanical alloying process parameters.**

| | |
|---|---|
| Rotation speed of disk (rpm) | 450 |
| Rotation speed of vial (rpm) | 500 |
| Ball material | Hardened carbon steel |
| Balls to powder weight ratio | 10:1 |
| Total powder mass (g) | 15 |

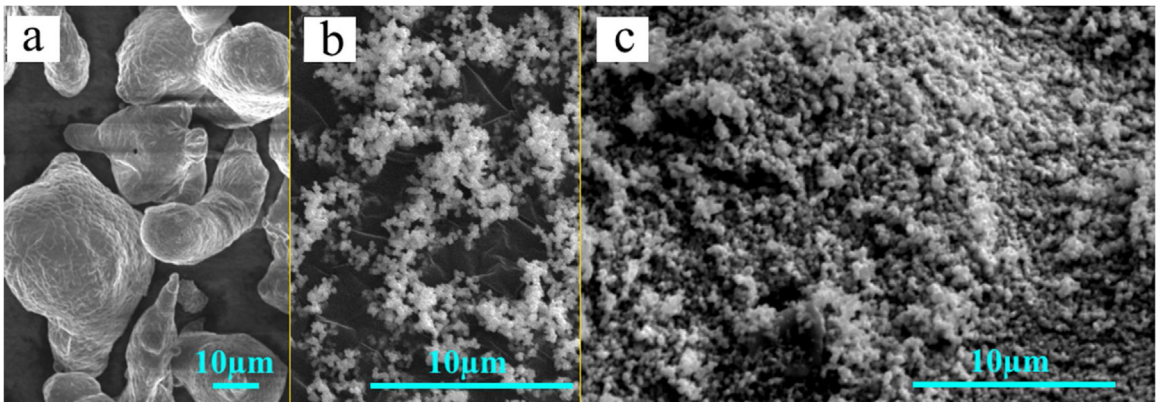


**Fig. 1 – SEM micrographs showing (a) the as-received Al, (b) $Fe_3O_4$ powders, and (c) the powder mixture after 1 h of milling.**

parameters. Rapidly after milling a double-layer titanium foil alongside with zirconium powder is used to wrap the powder product to avoid oxidation. Fig. 1(c) shows the morphology of the milled powder product after 1 h of milling. To prevent any powder oxidation, the FSP is done quickly after placing the milled product into the groove.

### 2.3. *Friction stir processing*

Inside the groove, which is prepared on specimens, are filled with the mixture powder (Fig. 2a), which is the product of mechanical alloying by using a vertical milling machine. After that, the samples are subjected to FSP when the grooves on the workpieces sealed carefully to capsulize the powder and to restrain powder dispersion during the process. The FSP utilized by overpassing a pin-less tool which is operated with 10 mm shoulder diameter and with 1120 rpm rotational ($w$) and 125 mm/min traversal speeds ($v$). Thereafter, the FSP is used for four passes were the process carried out with 100% overlapping using a H13 steel tool with 18 mm shoulder diameter, 5 mm pin diameter and 4 mm pin height (Fig. 2b). The pin had threads with a depth of 0.5 mm and angle of 30° with 2.5° nutation angle. The parameters are used for the FSP were $w = 1400$ rpm and $v = 40$ mm/min demonstrates details of the parameters suing during the FSP. To have a comparison sample, a workpiece is fabricated by using FSP without powder introduction when the same parameters are applied. An electronic top-view macro-image of the processed nanocomposite is shown in Fig. 2c, indicating a consistently processed specimen.

### 2.4. *Microstructural analyses*

The microstructural studies were performed on the specimens, which are collected from the FSPed workpieces by cutting sections transversely. The grinding and polishing stage is carried out up to the final polish step that performed by using the particular diamond paste and pad. Finally, the etching process on the specimens are performed using modified Poulton's reagent. The optical microscopy (OM; Olympus GX51), scanning electron microscopy (SEM; Jeol JSM-7600F) and transmission electron microscopy (TEM; Jeol 2000FX) are used to study the microstructural evolution. The SEM was equipped with energy-dispersive spectroscopy (EDS) and electron back-scattered diffraction (EBSD; Oxford Instruments, X-Max) detectors. Automatic grinding and polishing steps are employed as standard metallographic procedures and followed with a 45 min polishing step using colloidal silica to prepare the test samples for EBSD study. The Mambo and Tango software are used to process the EBSD data and plot misorientation distribution curves. As it is mentioned in the previous article during the EBSD study of different Al/oxide system, a cleanup procedure is used to re-index the data points. In this case, a cleanup with a 5° grain tolerance angle and 0.1 minimum confidence index (CI > 0.1) was applied to re-index the EBSD patterns. The misorientations in the range of 3–15° are considered as low-angle grain boundaries (LAGBs) which is indicated with bright contrast in EBSD images. Boundaries with higher angles were defined as high-angle grain boundaries (HAGBs), and they are illustrated with dark contrast in EBSD images. An X-ray diffraction (XRD) unit (Rigaku Ultima IV) is used to recognize the phases in fabricated composites within SZ. To collect the specimens for microscopy tests, the samples were removed with at least 30 mm distance from the FSP start/finish points.

## 3. Results and discussion

The ball milling process is used to provide an active and uniform mixture of powders from the initial powder mixture. The product powders have higher reaction kinetics during FSP. From first trials, it was concluded that utilizing the conventional mixing process is unsuccessful when dissimilar powders are using during mixing process since the density of $Fe_3O_4$ (4.8 g/cm$^3$) is much higher than aluminum (2.70 g/cm$^3$). Therefore, to achieve a uniform mixture of powders, the ball milling process was utilized according to the stoichiometric composition presented in Reaction (1). Fig. 3a indicates the XRD pattern of the milled Al–$Fe_3O_4$ powder mixture after 1 h milling. As can be seen, the individual Al and $Fe_3O_4$ peaks are the only ones which have been detected, illustrating that almost no reaction between Al and $Fe_3O_4$ took place during milling. The exception is related to the existence of peak broadening; this is related to reducing the crystallite size and extending the lattice strain. The milling time effect on

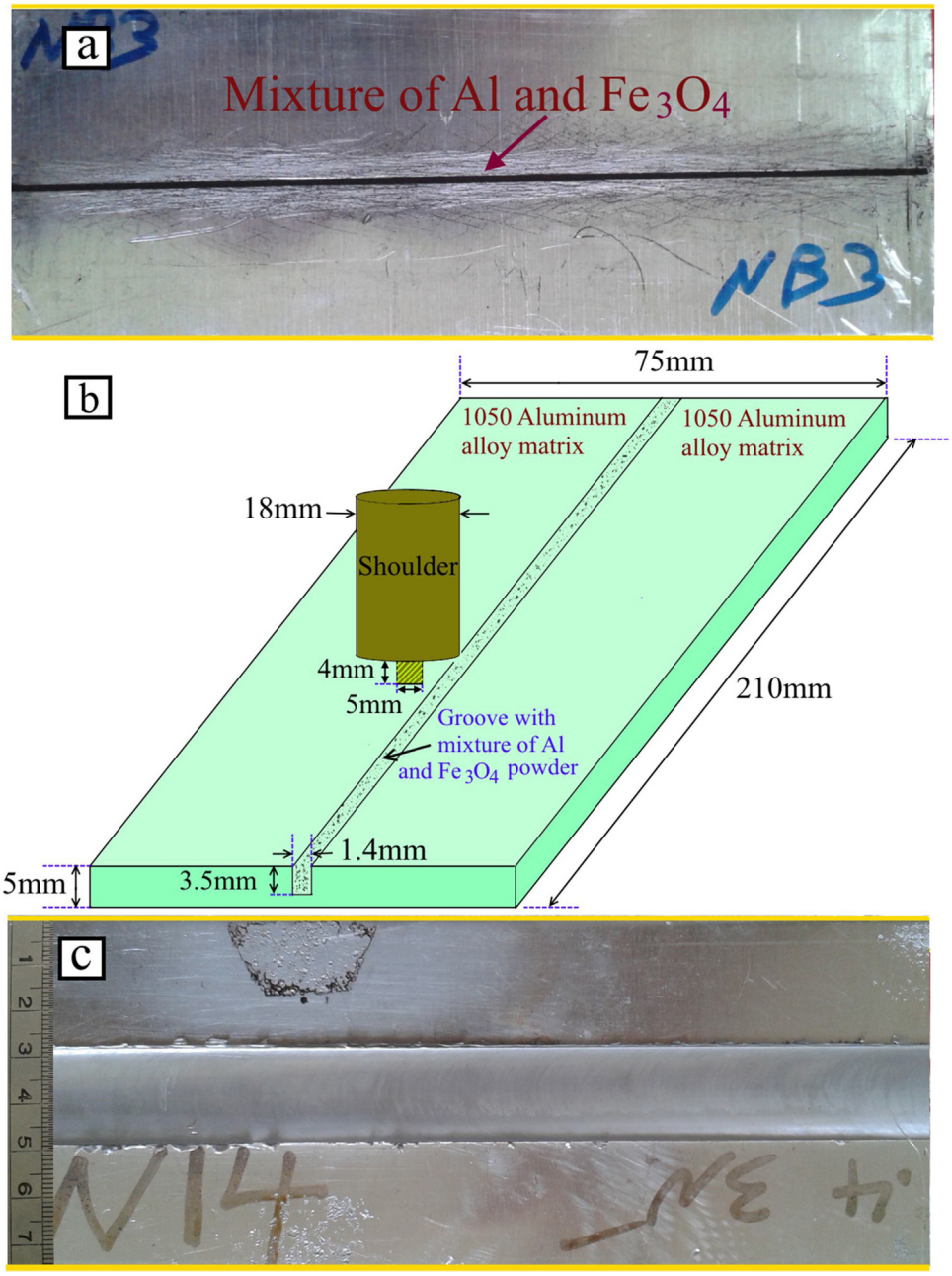


**Fig. 2 – (a) Specimen preparation for the FSP, (b) schematic of FSP accomplishment and (c) the prepared nanocomposite from the top view.**

$Fe_3O_4$–Al reaction determines by using differential thermal analysis (DTA) (Fig. 3b). It can be noticed that only the melting peak of aluminum at about 670 °C was revealed, specifying that no reaction occurred between Al and $Fe_3O_4$ after 1 h milling. As noted previously, to achieve a higher rate of reaction kinetics during FSP, the mechanical milling was employed to produce uniform and active powder mixture.

Fig. 4 shows the FE-SEM images related to FSPed AA1050 specimens with and without powder mixture addition. It demonstrates a fully uniform distribution of particles is achieved in the SZs of FSPed AA1050 after powder mixture addition, without any evidence of particle clustering (Fig. 4b). Generally, the composite is fabricated by the FSP in the SZ after adding the milled powder mixture. Fig. 4c illustrates FESEM micrographs and elemental mapping analyses for the friction stir processed nanocomposite specimen. It can be seen, different contrasts are displayed by the particles in the composite due to their matrix. As stated by the result of EDS analyses (point and elemental mapping probing), particles with light gray (1), pale gray (2), and bright (3) contrasts are steady iron aluminide compound, iron oxide, and aluminum oxide compositions, respectively. The formation of iron aluminide compound as a result of solid-state reactions of Al with $Fe_3O_4$ is notable.

Consequently, it becomes evident that the solid-state reaction between $Fe_3O_4$ particles and Al during FSP form Al–Fe

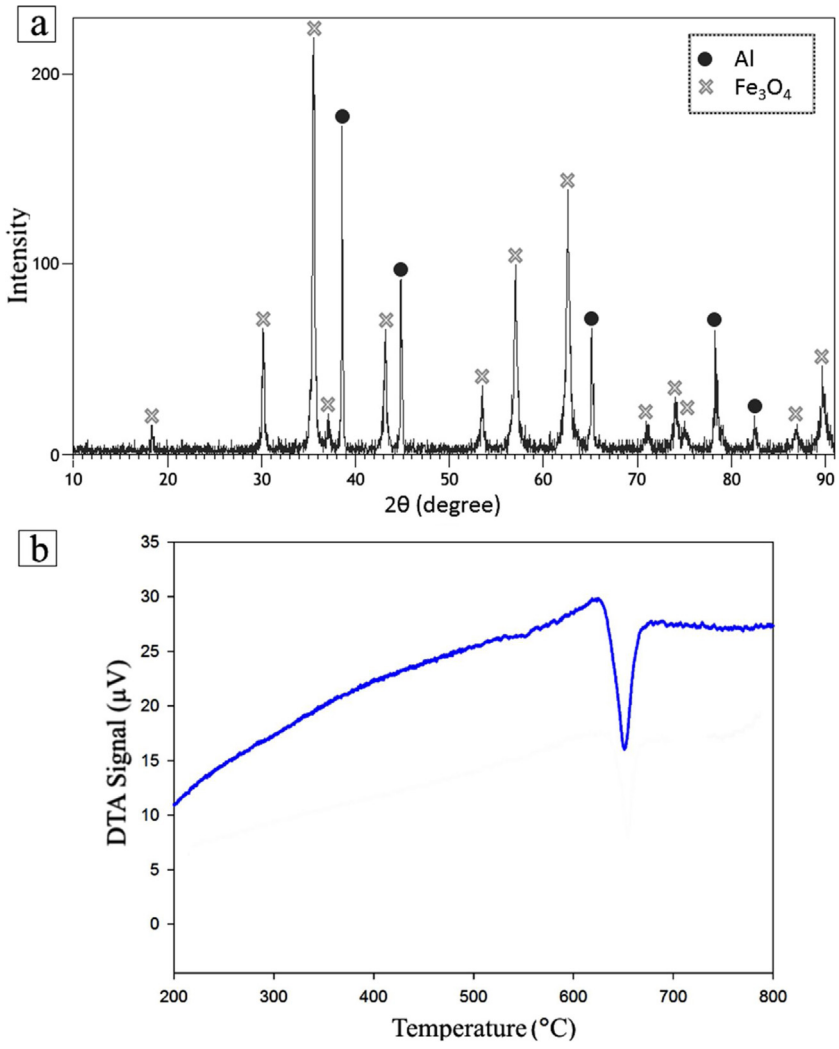


**Fig. 3 – (a) XRD pattern of the milled Al–$Fe_3O_4$ powder mixture, (b) DTA curve of Al–$Fe_3O_4$ powder mixture after 1 h of milling.**

intermetallic particles. It should be noticed that since two particles are small, it is difficult to detect them by the EDS, considering the resolution. It is suggested to use the chemical analyses based on qualitative elemental partitioning which can be described by partition coefficient as concentration ratio of an element between two phases, and it extracted from X-ray mapping instead of quantitative point analyses. As stated, the Al/$Fe_3O_4$ reaction occurs as the presence of particles is confirmed by the mentioned chemical analyses. Although the reaction is not kinetically finalized since even after four passes of FSP, the final produced composite contains some iron oxide particles.

X-ray diffraction experiments were carried out to investigate the fabricated phases after FSP. Fig. 5 shows the XRD patterns of AA1050 with powder addition. As can be seen, dominant Al, and minor phases peaks related to $Al_{13}Fe_4$, $Al_2O_3$ and $Fe_3O_4$ were detected. These results illustrate and prove that the reaction between Al and $Fe_3O_4$ took place during four pass FSP and in situ hybrid nanocomposite has been formed. Although the ratio of the peak intensity related to particles to compare with background intensity is low, the particles volume fraction is not very low (Fig. 4b). The appearance of low peak-to-background ratios is expected because of the nano-sized particles formation and the associated peak broadening effect. The correspondent diffraction patterns related to iron oxide showing that after four passes of FSP, the reaction between Al- $Fe_3O_4$ is not terminated.

Figs. 6–8 are exhibited the EBSD analyses of the microstructural details related to the as-rolled AA1050 base alloy and sinter zone of the FSPed samples with/without additional powder mixture. Also, Table 3 is presented the microstructural statistics for different specimens.

### 3.1. *Base metal*

Fig. 6(a)–(f) are included the main EBSD results for as-rolled AA1050 samples which are showing the grain boundary, grain orientation and recrystallization maps and misorientation angle distribution and restoration frequency histograms. Fig. 6c illustrated the grain boundaries when misorientation angles are larger than 15°. They highlighted by black color. White color is used for indication while the misorientation angles are lower than 15°. As it is mentioned before, the grain boundary with, misorientation angles larger and

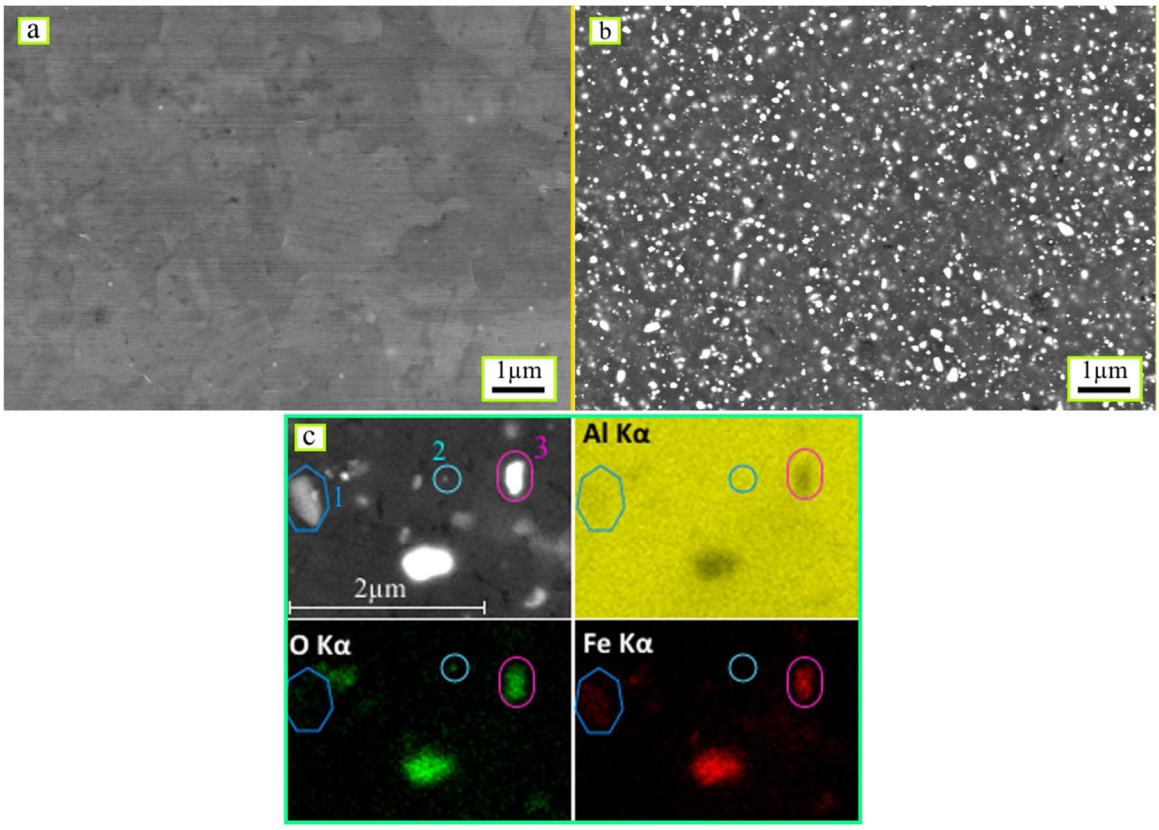


**Fig. 4 – SEM backscattered electron images of the SZs of FSPed AA1050 (a) without and (b) with Al–$Fe_3O_4$ powder addition (c) SEM micrograph and EDS X-ray maps of the fabricated composite using Al-Kα, O-Kα, and Fe-Kα radiations exhibiting elemental partitioning of 1, 2 and 3 type particles in Al matrix.**

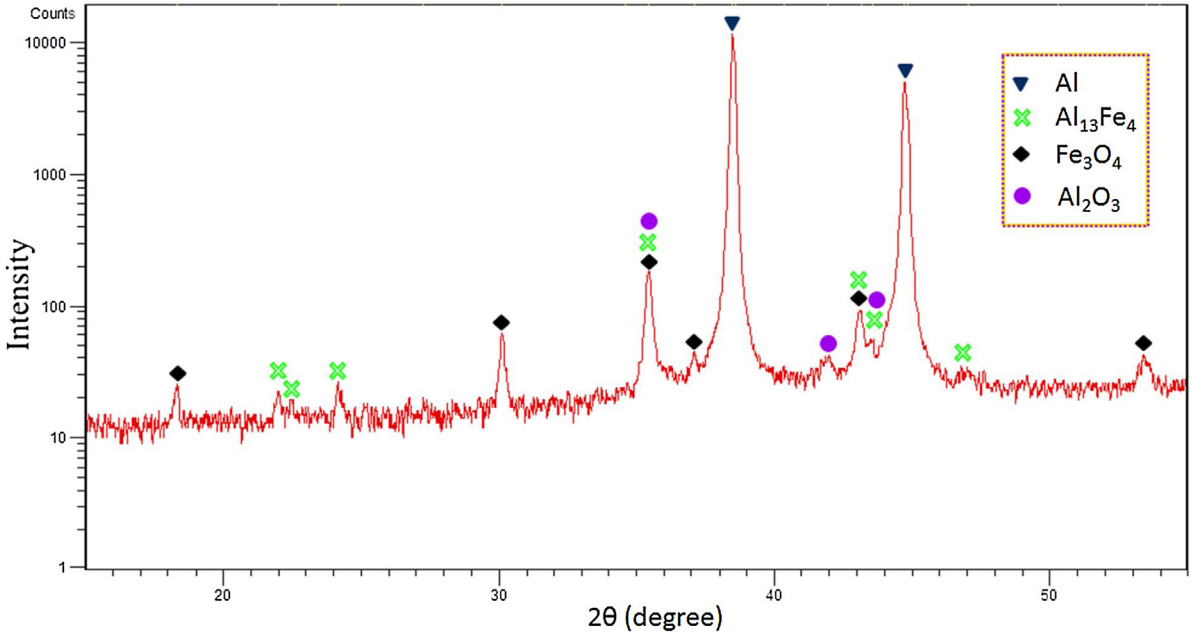


**Fig. 5 – X-ray diffraction pattern of the fabricated Al/($Al_{13}Fe_4$ + $Al_2O_3$) hybrid composite by FSP with Al–$Fe_3O_4$ powder mixture.**

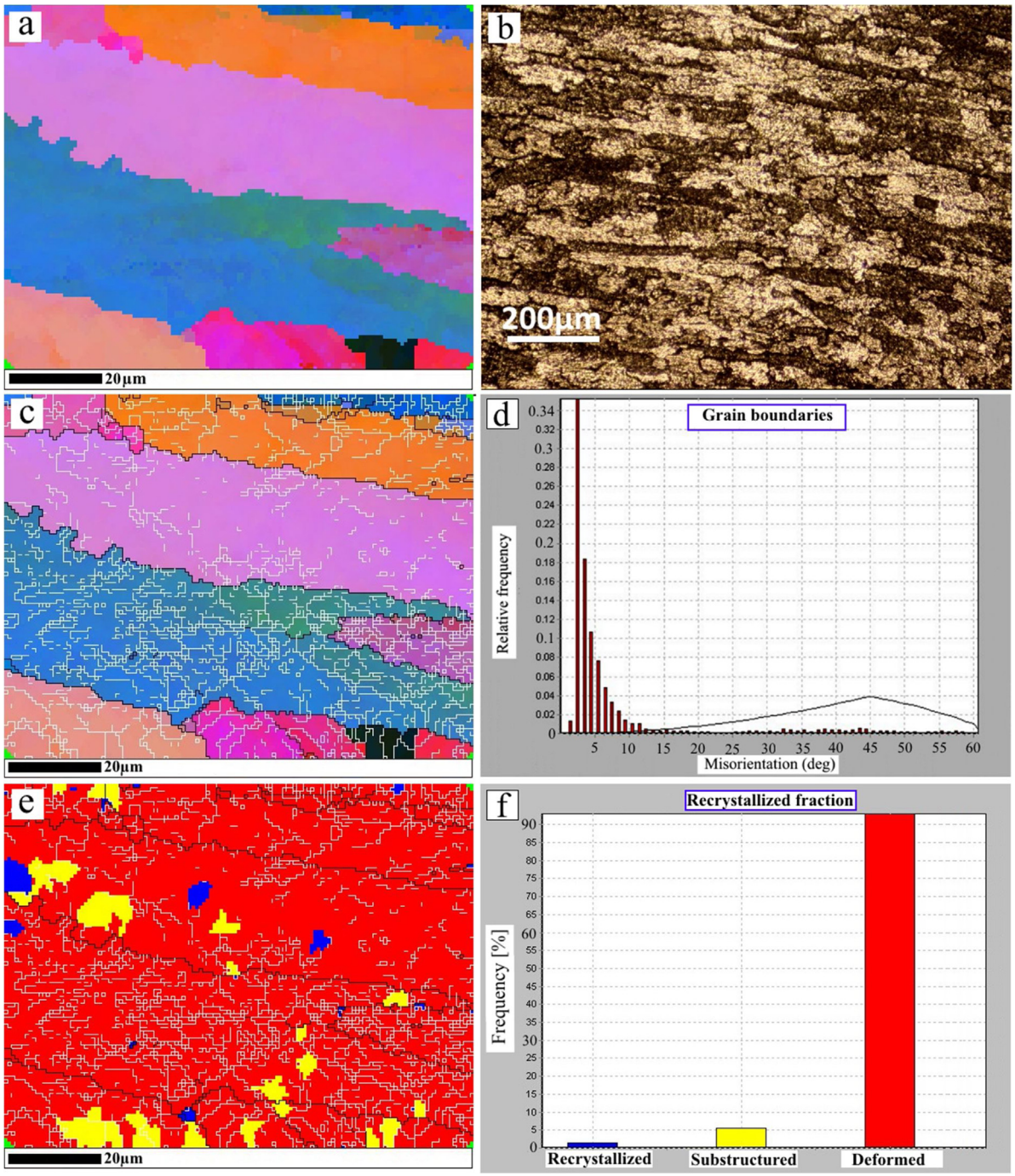


**Fig. 6 – (a) EBSD grain maps, (b) optical image of BM exhibiting a typical deformed microstructure, (c) orientation map (white color for LAGBs and black color for HAGBs), (d) misorientation angle distribution histogram, (e) recrystallization map and (F) restoration frequency histogram.**

**Table 3 – Microstructural details from different samples: average grain size ($d^{-}$, μm); fraction of LAGBs ($f_{LAGBs}$, %); fraction of HAGBs ($f_{HAGBs}$, %); fraction of recrystallized grains ($f_{RG}$, %); fraction of sub-structured grains ($f_{SG}$, %); fraction of deformed grains ($f_{DG}$, %); mean misorientation angle ($\theta$, degree).**

| Specimen | $d^{-}$ | $f_{LAGBs}$ | $f_{HAGBs}$ | $f_{RG}$ | $f_{SG}$ | $f_{DG}$ | $\theta$ |
|---|---|---|---|---|---|---|---|
| Base AA1050 | – | 89 | 11 | 1.5 | 5.5 | 93 | 31 |
| Without powder addition sample | 7.8 | 35 | 65 | 78 | 22 | – | 29.5 |
| With powder addition (composite sample) | 2.1 | 58 | 42 | 37 | 51 | 12 | 31.5 |

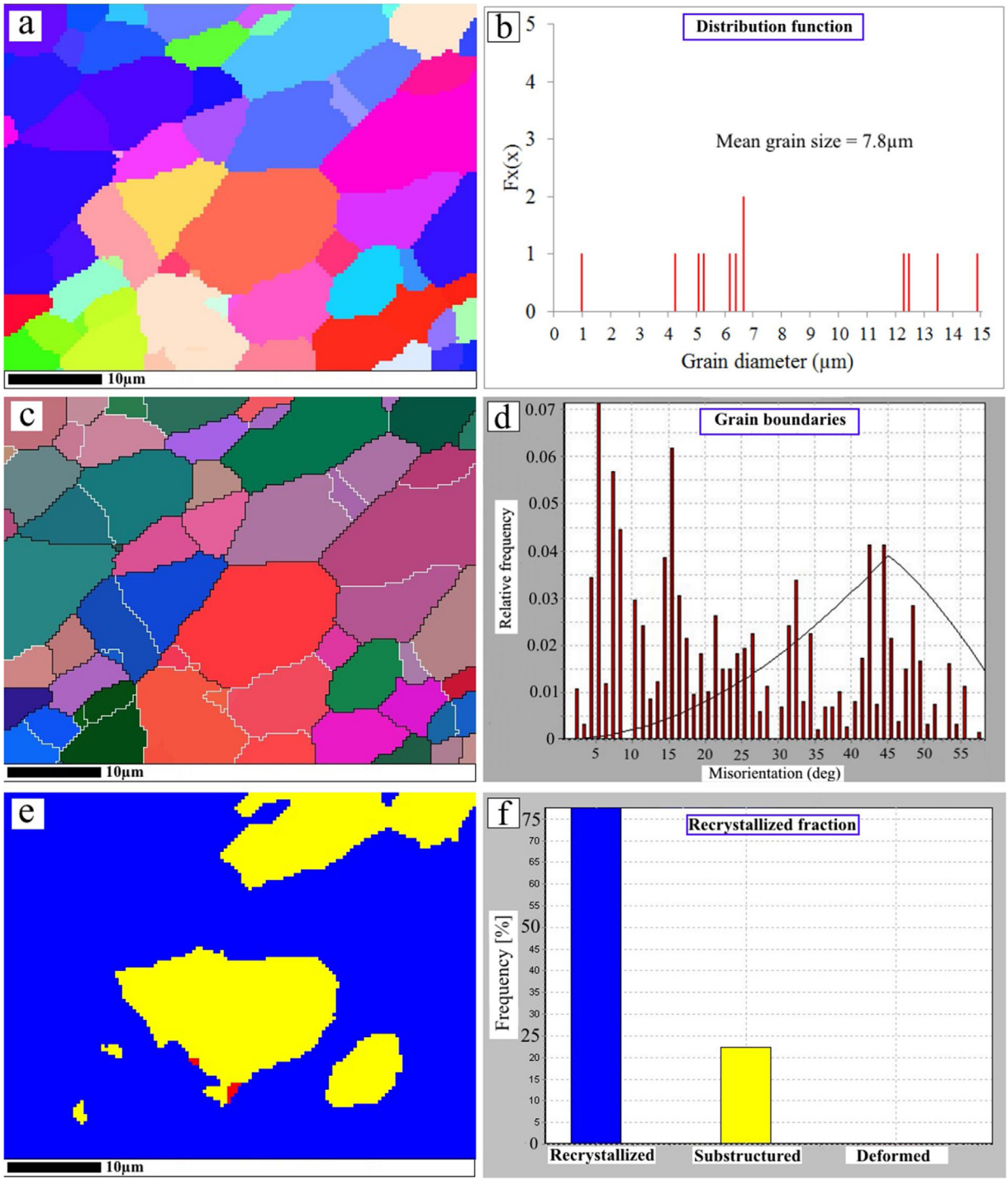


**Fig. 7 – The EBSD analysis results from SZ of the workpiece processed without powder addition; (a) grain boundary map, (b) grain size distribution histogram, (c) orientation map (white color for LAGBs and black color for HAGBs), (d) misorientation angle distribution histogram, (e) recrystallization map and (f) restoration frequency histogram.**

lower than 15° are known as HAGBs and LAGBs, respectively. This examined base material (BM) exhibit an elongated grains microstructure, a high ratio of LAGBs (~ 89%), a low proportion of recrystallized grains (~1%) and comparatively small misorientation angle (~31°). Fig. 6d shows the distribution histogram of the misorientation angle. The illustrated distribution is close to the random MacKenzie distribution curve while the plot of Fig. 6f shows a high fraction of deformed grains. These appearances are typical for the rolling microstructures.

### 3.2. *Effect of FSP*

By employing FSP, the equiaxed grains are formed with a mean size of ~7.8 μm, where the elongated grains of base

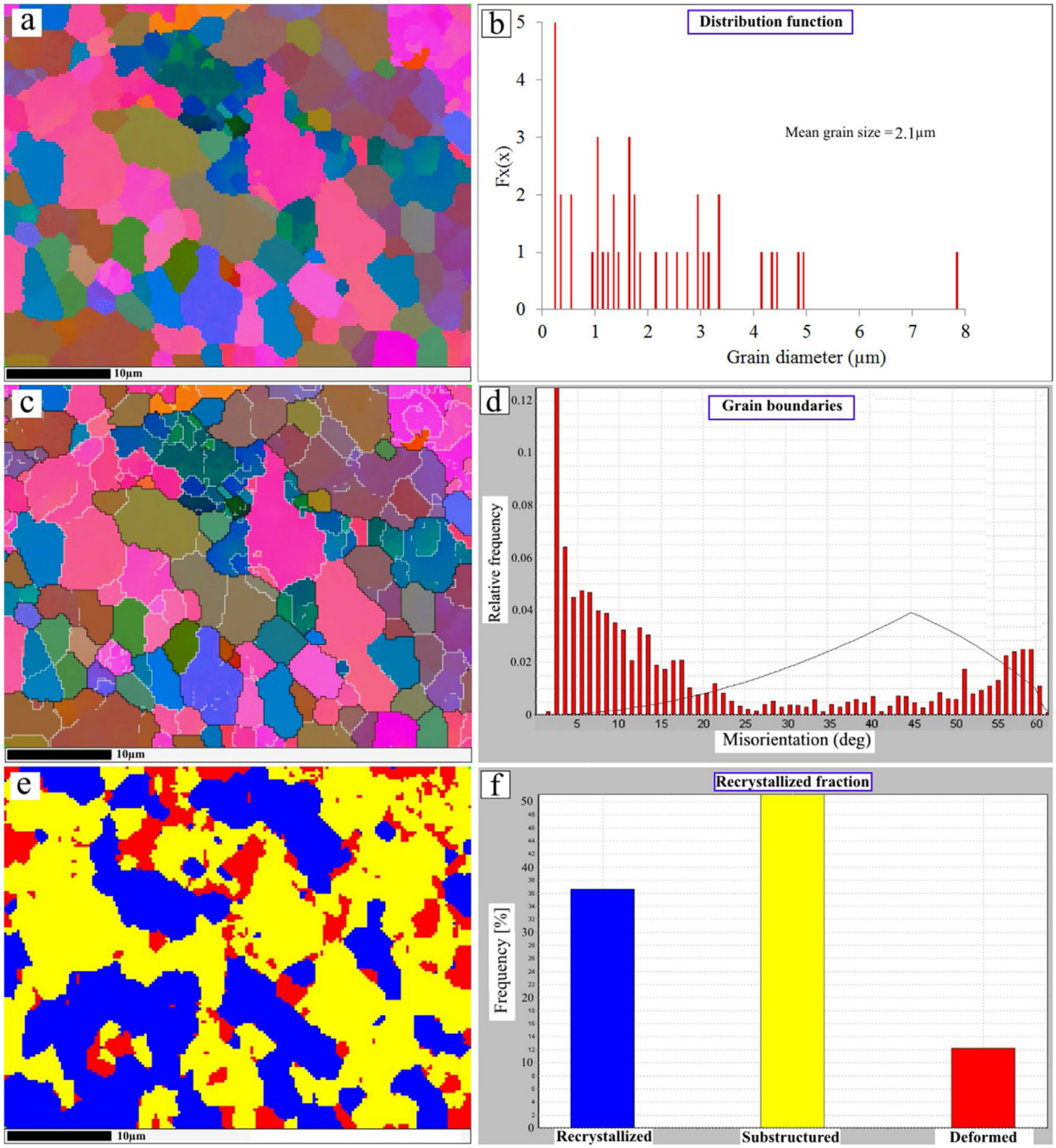


**Fig. 8 – The EBSD analysis results from SZ of the workpiece processed with Al + $Fe_3O_4$ addition (composite sample); (a) grain boundary map, (b) grain size distribution histogram, (c) orientation map (white color for LAGBs and black color for HAGBs), (d) misorientation angle distribution histogram, (e) recrystallization map and (f) restoration frequency histogram.**

materials (BM) were diminished (Fig. 7a–c). In fact, the formation of the equiaxed grain structure is due to the effect of dynamic restoration phenomena and happened after friction stir modification without the presence of particles. In addition, the mean misorientation angle is cut down in comparison with AA1050 base alloy from 31° to about 29.5°. It appears that the grains size are refined to sizes down to 7.8 μm due to severe plastic deformation while the high angle grain boundaries (HAGBs) have been formed because of dynamic recrystallization during FSP. Grain refinement happens in FSP/FSW due to existence of different dynamic restoration mechanisms [40].

Furthermore, During FSP, a high level of geometrically necessary dislocations (GND) density can be created. Those resulted in a complex stress field with a very large strain gradient. The high GND density leads to the strain incompatibilities which can be functioned as initial and preferred nucleation sites because of the dynamic restoration phenomena [12,40]. Besides that, it is apparent that the microstructure in the stir zone is mainly composed of an uncommon mixture of high

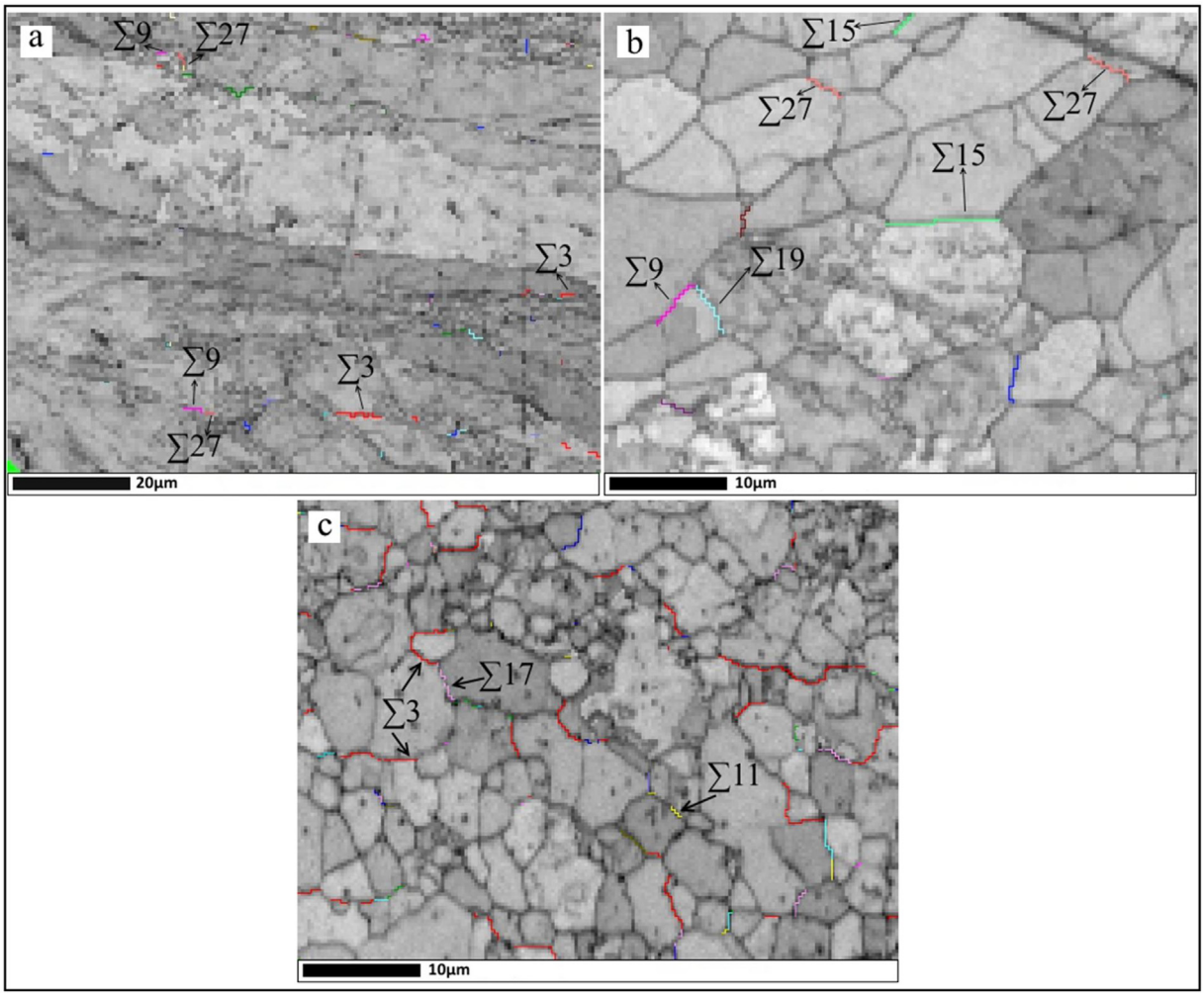


**Fig. 9 – EBSD maps of (a) AA1050 base alloy and SZs of the specimens (b) without and (c) with Al + $Fe_3O_4$ powder addition showing CSL boundaries.**

and low angles of grain boundaries. The deform microstructure will be consumed by new dynamically recrystallized grains; this has occurred when the new distinctive grains are formed from dynamic formation and extermination of LAGBs; in other words, the dynamic recrystallization is related to the transformation of sub-grains into new grains [41]. Eventually, it will be indicated that the fraction of LAGBs are reduced when correspondingly, the fraction of HAGBs are increased due to the formation of new individual grains. The increment of HAGBs number during dynamic recrystallization (DRX) is due to the continued dislocations accumulation in the subgrain boundaries when the misorientation is kept at a low level [29]. In fact, dynamic recrystallization Continuous (CDRX) occurs by the progressive accumulation of dislocations into LAGBs which increase their misorientation, and eventually, HAGBs are formed when the misorientation angles reach a critical value $\theta_c$ ($\theta_c \approx 15^\circ$) [27,42,43].

### 3.3. *Effect of powder addition*

Fig. 8 illustrates the EBSD mapping of the grain size and the orientation; also, contains the distribution histogram plots measured in the mid-thickness section for the nugget zone of the hybrid nanocomposite. Some other features can be noted such as the equiaxed grain structure that is formed with a mean grain size of 2.1 μm; and a slight increase that is occurred when the average misorientation angle is measured up to ~31.5°. The further increment has happened while the fraction of recrystallized grains reaches ~37%. In addition, the Al and $Fe_3O_4$ powder mixture has intensified grain refinements, and this is seen in the plots as the grain size distribution became narrow (Fig. 8a–c). Whereas the in situ precipitates is formed through changing the FSP to a reactive process by adding the milled powder. Those precipitates serve as reinforcements, and the matrix grains will refine by grain boundary pinning mechanism. These outcomes support the statement that the produced particles as a result of the reaction between Al and $Fe_3O_4$ had an extra effect on reducing the matrix grain size. As mentioned before, the presenting of various dynamic restoration mechanisms is the main reason for grain refinement happening during FSP/FSW. The static and dynamic restoration events can be affected significantly by the presence of nanoparticles, such as $Al_{13}Fe_4$ and $Al_2O_3$. Inserting inclusions during the process can make a higher

number of nucleation sites. It can happen at the beginning based on the particle stimulating nucleation (PSN) mechanism. An additional obstacle occurs on the short-range motion of grain boundaries, which conforms to the Zener–Smith Pinning mechanism [44]. All those lead to the formation of a finer structure from HAGBs during static conditions of heat treatments within heating or cooling cycles. Likewise, the increment of the grain refinement within the sintering zone along with multiplication of the preferred pinning sites occurs from hard ceramic particles production during reactive FSP and in situ phase formations.

A simple comparison between the EBSD results for the AA1050 base alloy and SZ regions of the FSPed specimen and hybrid nanocomposite can clarify the effects of adding milled powder on the microstructural details; it is shown in Figs. 6–8. The results show that the fraction of HAGBs is increased during FSP of both samples (with and without mixed powder). The grain refinement and recovery mechanisms engaged in an active competition during FSP that is related to the previous cold worked and microstructure of the rolled alloy. On the other hand, the modification of fine sub-grains structure is responsible for grain refinement, which occurs because of dislocations re-arrangements. The transformation of LAGBs into HAGBs in aluminum alloy happen as a result of the continuous dynamic recovery. This also involves progression and accumulation of dislocations at LAGBs [45,46].

### 3.4. *Effect of particles on coincident site lattice (CSL) notation*

There is reported in the literature that special boundaries are known as those boundaries with $\Sigma \leq 20$ [38]. The other boundaries, containing $\Sigma \geq 29$, are named as random. Using different categories for particular boundaries from random ones at Σ29 is based on the correlation between special fractions and observed properties. The special fraction calculates with dividing the total number of boundaries in the category of $1 \leq \Sigma \leq 29$ to the total number of boundaries [38]. The distribution of different types of the boundary with respect to $\Sigma$ is referred to the grain boundary character distribution (GBCD) term. It can be rigorously indicated that special boundaries (usually $\Sigma \leq 29$, especially $\Sigma 3^n$ ($n = 1$, 2, and 3)), which have low $\Sigma$ and happen at well-defined angles [47]. They exhibit exceptional properties in different classes such as kinetic, electronic, mechanical, chemical, and energy characteristics. Fig. 9 shows particular boundaries $\Sigma n$ in BM (1050 aluminum alloy), and FSPed specimens without and with $Fe_3O_4$/Al powder. Fig. 10 present quantitative approximation of different boundaries in all distinct specimens. The $\Sigma$ threshold, which the particular properties of grain boundaries can be lost above that, depends on the characterization method and investigated property. Pressure and mainly, temperature are among other external conditions that can affect the $\Sigma$ threshold [48]. Accordingly, the CSL boundaries are used to drive the fraction boundaries related to of Σ20, Σ29 and $\Sigma 3^n$ ($n = 1$, 2 and 3) which these derived data are summarized in Table 4.

Regarding the boundary fractions, it can attract the consideration that the numbers are very low for low ΣCSL boundaries related to BM (1050 aluminum alloy). As it is indicated in Table 4, for $\Sigma \leq 20$ boundaries, the fraction number is only about 0.7%. It is observed that in the comparison between BM and without powder FSPed specimens, the fraction of low ΣCSL boundaries increased due to the FSP. The interaction of pre-existing Σ3 boundaries through grain boundary migration, which is happened during dynamic restoration mechanisms, may form new Σ3 boundaries. Different investigation [30,31,49] mentioned that the atomic interaction forms the new boundaries. These interactions associated with grain boundary migration phenomena during DRX.

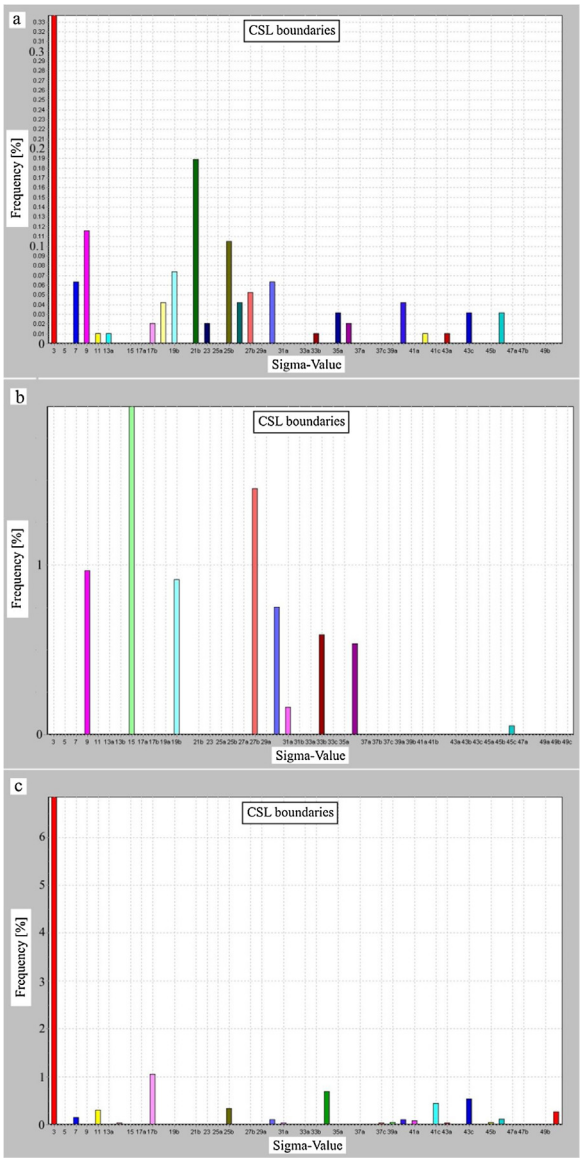


**Fig. 10 – Grain boundary character distribution (CSL) for (a) AA1050 base alloy and SZs of the specimens (b) without and (c) with Al + $Fe_3O_4$ powder addition.**

On the other hand, as can be seen in Fig. 10 and Table 4, the fraction of low ΣCSL boundaries is enhanced by adding the milled powder mixture (Al and $Fe_3O_4$). Therefore, it can be expressed that some other effective mechanisms on dynamic recrystallization will activate by the presence of nanoparticles. Grain boundary pinning and Particle-stimulated nucleation (PSN) are examples for those effectual mechanisms on DRX

**Table 4 – The fraction of low ΣCSL boundaries derived from the CSL boundaries.**

| Specimen | Boundaries with $\Sigma \leq 20$ (%) | Boundaries with $\Sigma \leq 29$ (%) | Boundaries with $\Sigma 3^n$ ($n = 1, 2$ and 3) (%) |
|---|---|---|---|
| Base AA1050 | 0.675 | 1.08 | 0.51 |
| FSPed AA1050 without powder | 3.8 | 5.3 | 2.42 |
| Hybrid nano-composite | 8.34 | 8.67 | 8.34 |

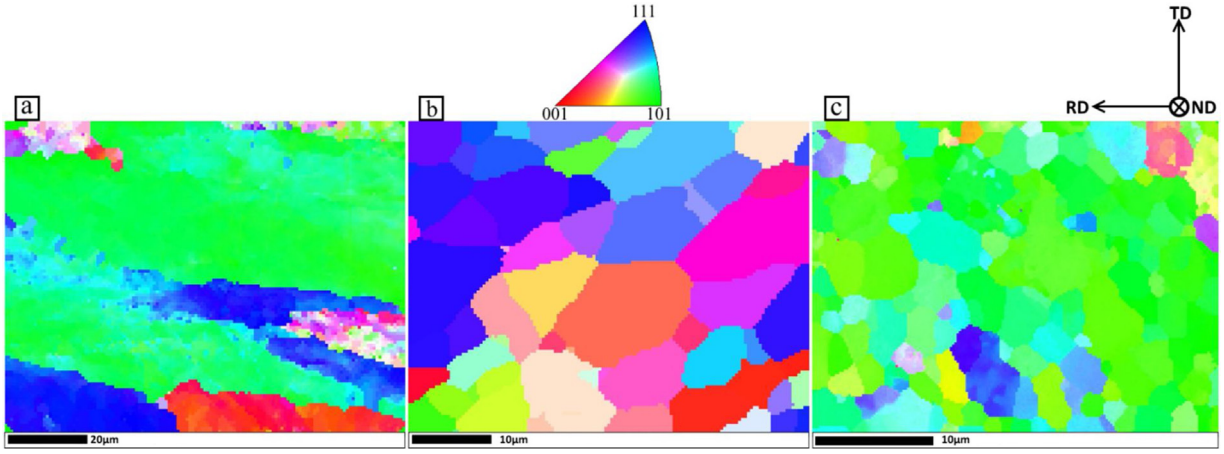


**Fig. 11 – Inverse pole figure coloring maps of (a) AA1050 base alloy and SZs of the specimens (b) without and (c) with Al + $Fe_3O_4$ powder addition.**

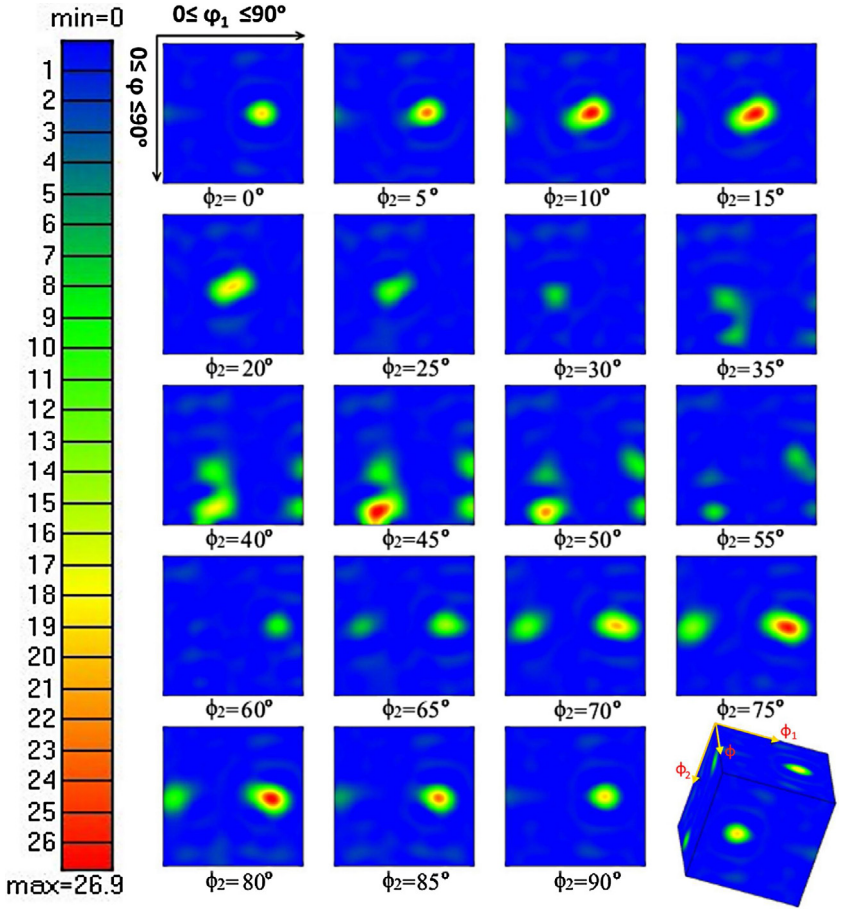


**Fig. 12 – ODF plotted at constant $\phi_2$ cross-sections of the Euler space showing texture components for BM (1050 aluminum alloy).**

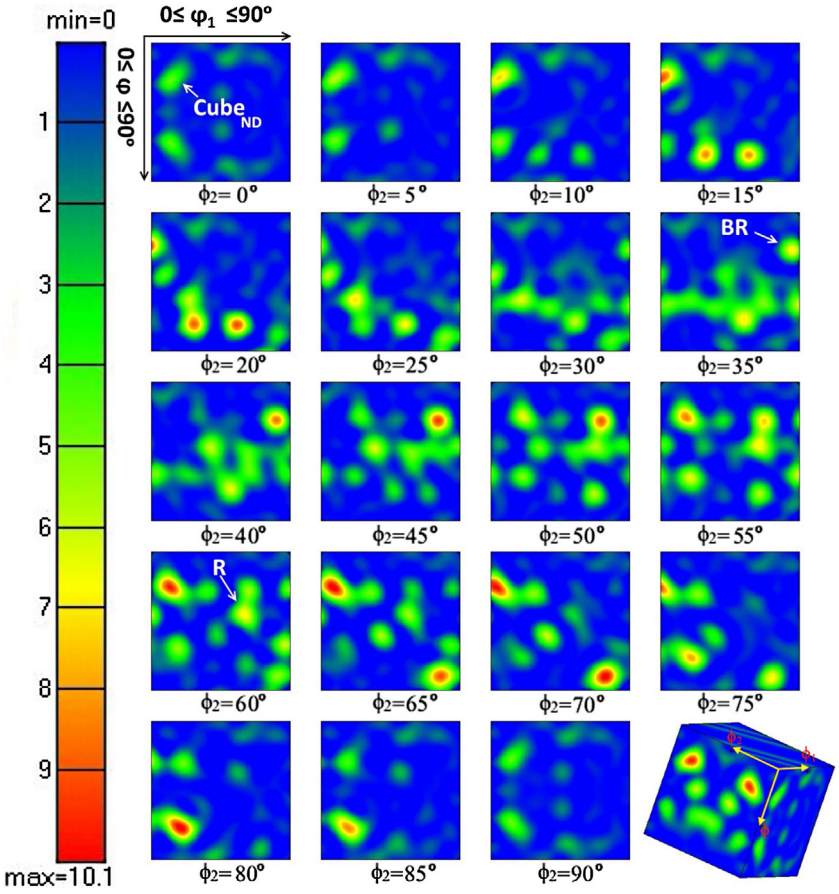


**Fig. 13 – ODF plotted at constant ϕ2 cross-sections of the Euler space showing texture components for workpiece processed without powder addition.**

[50,51]. Altogether, for those reasons, the higher fraction of low ΣCSL boundaries can form, and it follows by grains refinement.

The thermal exposure during FSP and the severe plastic deformation as nature of the process can form fine recrystallized grain structure and establish a specific texture [52,53]. During FSP, the texture is developed mainly because of the active deformation mechanisms and microstructure transformation caused by restoration phenomena. It is expected to observe the formation of diverse texture components in the microstructure because of different response by grains of SZ to the imposed strain and temperature. On the other hand, the stacking fault energy (SFE) is comparatively high for F.C.C metals and alloys such as aluminum and its alloys. The high SFE has a strong effect on the operating dynamic restoration mechanisms which is recovery and recrystallization during FSP, and it will control the resulting deformation textures [46]. The inverse pole figure (IPF) coloring maps is presented in Fig. 11. The figure relates to BM, FSPed without inserting the milled powder and hybrid nanocomposite samples. IPF maps show the crystallographic orientations for individual grains with respect to the rolling direction (RD). The color code for orientation parallel to the RD axis is given in the basic triangle at the top right corner. The colors in the IPF map are same when the neighboring grains have the identical orientations. It can be seen that the rolled structure is characteristic for the 1050 aluminum alloy which indicate an intense rolling process performed on specimens. For the FSPed specimens the IPF map shows variations of preferential grain orientations.

Figs. 12–14 show the orientation distribution functions (ODFs) of the specimens were concluded from the EBSD results. They are used to analyze the consequence of FSP and powder addition on the crystallographic texture evolution of the 1050 aluminum alloy.

Fig. 12 shows the analyses of ODF maps related to BM that is marked a typical rolling texture for wrought 1050 aluminum alloy. Fig. 13 shows the main texture development in FSPed sample (without additional powder) are constituted of $Cube_{ND}$ [54] ⟨310⟩, BR{236}⟨385⟩ and R (or retained S{123}⟨634⟩). The $Cube_{ND}$ component has a proximate 40°⟨111⟩ rotation regarding Cu orientation. The effect of concurrent precipitation can bring the advantage in growth rate for the $Cube_{ND}$ in comparison to the other orientations [55]. The incubation time related to $Cube_{ND}$ is shorter to compare with other orientations. This shorter time affects in less precipitation upon these nuclei. It is often to observe the R texture after annealing of cold rolled commercial metal aluminum and specified alloys. It is usually known as retained rolling texture. The reason for such referral is the similarity to the S deformation texture.

Fig. 14 shows the ODF maps related to hybrid nanocomposite. The microtextural evolution within the SZ of hybrid nanocomposite is different. The dominant component is only

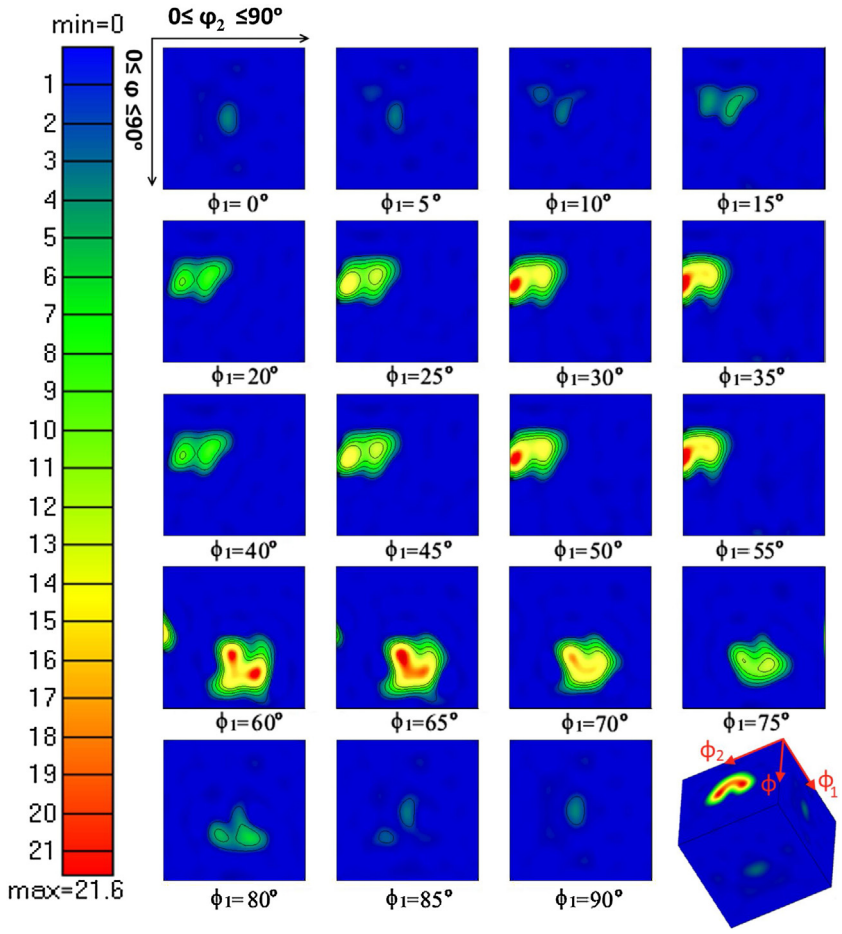


**Fig. 14 – ODF plotted at constant $\phi_2$ cross-sections of the Euler space showing texture components for hybrid nanocomposite.**

$Cube_{Twin}$. It is mentioned before that the particle stimulating nucleation (PSN) and pinning mechanisms during dynamic recrystallization (DRX) are affected by the presence and distribution of hard nanoparticles, which results in the texture development. On the other hand, incorporation of nanoparticles such as $Al_{13}Fe_4$ and $Al_2O_3$ throughout the matrix changes the shear textures to $Cube_{Twin}$ component. The most generalized recrystallization texture to compare with other textures is the cube component. With noticing that DRX nucleation can initiate from cube bands composed by onion-ring flow pattern of nanoparticles; continue with changing the shear direction during stirring motion of rotary tool during FSP which can enhance the chance of inducing C texture component at the sintering zone of hybrid nanocomposite specimen [56]. The partial completion of DRX in the nugget zone, promoted by hard nanoparticles and precipitates can cause the change of texture components in the sintering zone of the nanocomposite sample.

Table 5 demonstrates the texture intensity and fractions of HAGBs and LAGBs. The correlation between the fraction ratio of HAGBs and LAGBs and texture strength is presented in Table 5 after careful evaluation and data comparison. In other words, the grain boundaries evolution and texture transition within the SZ has a close relation to each other. This is apparent that hybrid nanocomposite to compare with FSPed AA1050 sample without additional powder shows higher-strength texture and LAGBs fraction (lower fraction of HAGBs). Generally, a high texture strength is the result of slight differences in crystallographic orientation of a large number of grains. The term strong texture means that the

**Table 5 – HAGBs and LAGBs fractions and texture intensity in the central regions of FSPed AA1050 (a) without and (b) with Al-$Fe_3O_4$ powder addition, obtained from EBSD texture data.**

| Specimen | HAGBs fraction,% | LAGBs fraction,% | Texture intensity |
|---|---|---|---|
| FSPed AA1050 without powder | 65 | 35 | 10.1 |
| Hybrid nano-composite | 42 | 58 | 21.6 |

orientations of neighbor grains are close to each other, or it can be expressed as the dissimilarity between the orientations of adjacent grains (Fig. 11). In this case, the boundary that exists between adjacent grains is classifying as a low-angle boundary. Consequently, analyzing the texture is one important parameter and significant tools to characterize the grain size, grain orientation, and type of grain boundaries.

## 4. Summary

In situ Al/($Al_{13}Fe_4$ + $Al_2O_3$) hybrid nanocomposite was synthesized by using multi-passes overlapping FSP when the milled powder mixture of $Fe_3O_4$ and Al insert to the stir zone, and a reduction reaction is applied. The fabricated hybrid nanocomposite was studied in terms of the microstructure evolution, transformation of grain boundaries and different variation of texture and compared to those of the BM and FSPed 1050 aluminum alloy (without the introduction of additional powder). The obtained results can be summarized as follows:

The in situ formation and scattering of nanoparticles in the aluminum matrix accelerate the dynamic restoration process; also, it can act as a significant hinder on the grain growth during dynamic recrystallization; finally, it can result in the reduction of grain size. The average grain size of the hybrid nanocomposite was about 2.1 μm.

The high angle grain boundaries (HAGBs) fraction in the SZ increase during FSP, and it is an indicator of the dynamic restoration process.

The fraction of $\Sigma 3^n$ boundaries increased by FSP, which indicated that a greater part of Σ3 boundaries are newly nucleated during restoration process.

The addition of milled (Al + $Fe_3O_4$) powder mixture and formation of hard nanoparticles intensify the fraction of low ΣCSL boundaries.

The main recrystallization texture components change to cube texture component by the presence of nanoparticles in the fabricated hybrid nanocomposite.

## Conflicts of interest

The authors declare no conflicts of interest.

## Acknowledgements

The authors the express gratitude acknowledge the Iran National Science Foundation (under the project no. 94004765), Iran Nanotechnology Initiative Council, Slovak Academy of Sciences (Institute of Materials & Machine Mechanics, Slovak Foundation VEGA Grant 2_0158_16, and by Grant APVV-14-0936), the UK EPSRC CAMREG funded project (Ref. No. EP/P007805/1).

REFERENCES

[1] Taherzadeh Mousavian R, Azari Khosroshahi R, Yazdani S, Brabazon D, Boostani AF. Fabrication of aluminum matrix composites reinforced with nano- to micrometer-sized SiC particles. Mater Design 2016;89:58–70.

[2] Palanivel R, Dinaharan I, Laubscher RF, Davim JP. Influence of boron nitride nanoparticles on microstructure and wear behavior of AA6082/TiB2 hybrid aluminum composites synthesized by friction stir processing. Mater Design 2016;106:195–204.

[3] Ramnath BV, et al. Aluminium metal matrix composites – a review. Rev Adv Mater Sci 2014;38(5):55–60.

[4] Mishra RS, Ma ZY, Charit I. Friction stir processing: a novel technique for fabrication of surface composite. Mater Sci Eng A 2003;341(1):307–10.

[5] Selvam JDR, Dinaharan I, Philip SV, Mashinini P. Microstructure and mechanical characterization of in situ synthesized AA6061/($TiB_2$ + $Al_2O_3$) hybrid aluminum matrix composites. J Alloys Compds 2018;740:529–35.

[6] El-Sabbagh AM, Soliman M, Taha MA, Palkowski H. Effect of rolling and heat treatment on tensile behaviour of wrought Al–SiCp composites prepared by stir-casting. J Mater Process Technol 2013;213(10):1669–81.

[7] Khan M, Zulfaqar M, Ali F, Subhani T. Hybrid aluminium matrix composites containing boron carbide and quasicrystals: manufacturing and characterisation. Mater Sci Technol 2017;33(16):1955–63.

[8] Chen W, Liu Y, Yang C, Zhu D, Li Y. (SiCp + Ti)/7075Al hybrid composites with high strength and large plasticity fabricated by squeeze casting. Mater Sci Eng A 2014;609:250–4.

[9] Monazzah AH, Bagheri R, Reihani SS, Pouraliakbar H. Toughness enhancement in architecturally modified Al6061–5 vol.%SiCp laminated composites. Int J Damage Mech 2015;24(2):245–62.

[10] Pouraliakbar H, et al. Toughness prediction in functionally graded Al6061/SiCp composites produced by roll-bonding. Ceram Int 2014;40(6):8809–25.

[11] Pouraliakbar H, Nazari A, Fataei P, Livary AK, Jandaghi M. Predicting Charpy impact energy of Al6061/SiCp laminated nanocomposites in crack divider and crack arrester forms. Ceram Int 2013;39(6):6099–106.

[12] Mishra RS, Ma Z. Friction stir welding and processing. Mater Sci Eng R: Rep 2005;50(1-2):1–78.

[13] Sharma V, Prakash U, Kumar BM. Surface composites by friction stir processing: a review. J Mater Process Technol 2015;224:117–34.

[14] Azimi-Roeen G, Kashani-Bozorg SF, Nosko M, Švec P. Reactive mechanism and mechanical properties of in-situ hybrid nano-composites fabricated from an Al–$Fe_2O_3$ system by friction stir processing. Mater Charact 2017;127:279–87.

[15] Chen C, Kao P, Chang L, Ho N. Effect of processing parameters on microstructure and mechanical properties of an Al–$Al_{11}Ce_3$–$Al_2O_3$ in-situ composite produced by friction stir processing. Metall Mater Trans A 2010;41(2):513–22.

[16] Hsu C, Kao P, Ho N. Intermetallic-reinforced aluminum matrix composites produced in situ by friction stir processing. Mater Lett 2007;61(6):1315–8.

[17] Khodabakhshi F, Simchi A, Kokabi A, Sadeghahmadi M, Gerlich A. Reactive friction stir processing of AA 5052–$TiO_2$ nanocomposite: process–microstructure–mechanical characteristics. Mater Sci Technol 2015;31(4):426–35.

[18] Madhu H, Kumar PA, Perugu CS, Kailas SV. Microstructure and mechanical properties of friction stir process derived Al–$TiO_2$ nanocomposite. J Mater Eng Perform 2018;27(3):1318–26.

[19] Zhang Q, Xiao B, Wang Q, Ma Z. In situ $Al_3Ti$ and $Al_2O_3$ nanoparticles reinforced Al composites produced by friction stir processing in an Al–$TiO_2$ system. Mater Lett 2011;65(13):2070–2.

[20] Zhang Q, Xiao B, Wang W, Ma Z. Reactive mechanism and mechanical properties of in situ composites fabricated from

an Al–$TiO_2$ system by friction stir processing. Acta Mater 2012;60(20):7090–103.
[21] You G, Ho N, Kao P. The microstructure and mechanical properties of an Al–CuO in-situ composite produced using friction stir processing. Mater Lett 2013;90:26–9.
[22] AzimiRoeen G, Kashani-Bozorg SF, Nosko M, Lotfian S. Mechanical and microstructural characterization of hybrid aluminum nanocomposites synthesized from an Al–$Fe_3O_4$ system by friction stir processing. Metals Mater Int 2019:1–13.
[23] Bayraktar E, Katundi D. Development of a new aluminium matrix composite reinforced with iron oxide (Fe; 2010.
[24] Botta P, Bercoff P, Aglietti E, Bertorello H, López JP. Magnetic and structural study of mechanochemical reactions in the Al–$Fe_3O_4$ system. J Mater Sci 2002;37(12):2563–8.
[25] Woo W, Choo H, Brown D, Vogel S, Liaw P, Feng Z. Texture analysis of a friction stir processed 6061-T6 aluminum alloy using neutron diffraction. Acta Mater 2006;54(15):3871–82.
[26] Fonda R, Knipling K. Texture development in friction stir welds. Sci Technol Weld Join 2011;16(4):288–94.
[27] Huang K, Logé R. A review of dynamic recrystallization phenomena in metallic materials. Mater Design 2016;111:548–74.
[28] Tancret F, Galindo-Nava E, Díaz-Del PEJR. Dynamic recrystallisation model in precipitation-hardened superalloys as a tool for the joint design of alloys and forming processes. Mater Design 2016;103:293–9.
[29] Azimi-roeen G, Kashani-bozorg SF, Nosko M, Orovcik L. EBSD investigation of Al/($Al_{13}Fe_4$ + $Al_2O_3$) nanocomposites fabricated by mechanical milling and friction stir processing. J Microsc 2018;270(1):3–16.
[30] Khodabakhshi F, Nosko M, Gerlich A. Influence of CNTs decomposition during reactive friction-stir processing of an Al–Mg alloy on the correlation between microstructural characteristics and microtextural components. J Microsc 2018.
[31] Cao Y, Di H, Zhang J, Zhang J, Ma T, Misra R. An electron backscattered diffraction study on the dynamic recrystallization behavior of a nickel–chromium alloy (800H) during hot deformation. Mater Sci Eng A 2013;585:71–85.
[32] Kronberg M, Wilson uF. Secondary recrystallization in copper. JOM 1949;1(8):501–14.
[33] Lejček P. Grain boundaries: description, structure and thermodynamics. In: Grain boundary segregation in metals. Berlin, Heidelberg: Springer; 2010, pp 5–24.
[34] Randle V. The measurement of grain boundary geometry. Routledge; 2017.
[35] Winning M, Gottstein G, Shvindlerman LS. On the mechanisms of grain boundary migration. Acta Mater 2002;50(2):353–63, 2002/01/22/.
[36] Shimokawa T, Niiyama T, Okabe M, Sawakoshi J. Interfacial-dislocation-controlled deformation and fracture in nanolayered composites: toward higher ductility of drawn pearlite. Acta Mater 2019;164:602–17.
[37] Vattré A, Pan E. Semicoherent heterophase interfaces with core-spreading dislocation structures in magneto-electro-elastic multilayers under external surface loads. J Mech Phys Solids 2019;124:929–56.
[38] Palumbo G, Aust K. Solute effects in grain boundary engineering. Can Metallur Quart 1995;34(3):165–73.
[39] Shi F, Li X, Hu Y, Su C, Liu C. Optimization of grain boundary character distribution in Fe–18Cr–18Mn–0.63N high-nitrogen austenitic stainless steel. Acta Metallur Sinica (Eng Lett) 2013;26(5):497–502.
[40] Sakai T, Belyakov A, Kaibyshev R, Miura H, Jonas JJ. Dynamic and post-dynamic recrystallization under hot, cold and severe plastic deformation conditions. Progress Mater Sci 2014;60:130–207.
[41] Rao A, et al. Recrystallization phenomena during friction stir processing of hypereutectic aluminum-silicon alloy. Metallur Mater Trans A 2013;44(3):1519–29.
[42] Gourdet S, Montheillet F. An experimental study of the recrystallization mechanism during hot deformation of aluminium. Mater Sci Eng A 2000;283(1-2):274–88.
[43] Kaibyshev R, Shipilova K, Musin F, Motohashi Y. Continuous dynamic recrystallization in an Al–Li–Mg–Sc alloy during equal-channel angular extrusion. Mater Sci Eng A 2005;396(1-2):341–51.
[44] Nosko M, et al. Solid-state joining of powder metallurgy Al–$Al_2O_3$ nanocomposites via friction-stir welding: effects of powder particle size on the weldability, microstructure, and mechanical property. Mater Sci Eng A 2019;754:190–204.
[45] Khodabakhshi F, Simchi A, Kokabi A, Gerlich A, Nosko M. Effects of stored strain energy on restoration mechanisms and texture components in an aluminum–magnesium alloy prepared by friction stir processing. Mater Sci Eng A 2015;642:204–14.
[46] McNelley T, Swaminathan S, Su J. Recrystallization mechanisms during friction stir welding/processing of aluminum alloys. Scripta Mater 2008;58(5):349–54.
[47] Adams BL, Zhao J, Grimmer H. Discussion of the representation of intercrystalline misorientation in cubic materials. Acta Crystallogr Sec A 1990;46(7):620–2.
[48] Doherty R, et al. Current issues in recrystallization: a review. Mater Today 1998;1(2):14–5.
[49] Shamanian M, Mostaan H, Safari M, Szpunar JA. EBSD study on grain boundary and microtexture evolutions during friction stir processing of A413 cast aluminum alloy. J Mater Eng Perform 2016;25(7):2824–35.
[50] Troeger L, Starke E Jr. Particle-stimulated nucleation of recrystallization for grain-size control and superplasticity in an Al–Mg–Si–Cu alloy. Mater Sci Eng A 2000;293(1-2):19–29.
[51] Chang C, Lee C, Huang J. Relationship between grain size and Zener–Holloman parameter during friction stir processing in AZ31 Mg alloys. Scripta Mater 2004;51(6):509–14.
[52] Fonda R, Bingert J. Texture variations in an aluminum friction stir weld. Scripta Mater 2007;57(11):1052–5.
[53] Shafiei-Zarghani A, Kashani-Bozorg SF, Gerlich AP. Texture analyses of Ti/$Al_2O_3$ nanocomposite produced using friction stir processing. Metall Mater Trans A 2016;47(11):5618–29.
[54] !!! PLEASE PROVIDE COMPLETE REFERENCE DETAILS !!!.
[55] Daaland O, Dronen P-E, Vatne HE, Naess S, Nes E. On the growth rate of cube-, rotated cube-and rotated goss-grains in commercial aluminium alloys. Mater Sci Forum 1993;113:115–20.
[56] Khodabakhshi F, Nosko M, Gerlich A. Dynamic restoration and crystallographic texture of a friction-stir processed Al–Mg–SiC surface nanocomposite. Mater Sci Technol 2018;34(14):1773–91.